Reinforced copper matrix composites with highly dispersed nano size TiC *in situ* generated from the Carbon Polymer Dots

Xiao Huang[1], Longke Bao[2], Rui Bao[1]*, Liang Liu[1]**, Jingmei Tao[1], Jinsong Wang[1], Zhengfu Zhang[1], Zhenhua Ge[1], Songlin Tan[1], Jianhong Yi[1], Fanran Meng[3]

1. Faculty of Materials Science and Engineering, Kunming University of Science and Technology, Kunming 650093, China

2. Institute of Materials Genome and Big Data, Harbin Institute of Technology, Shenzhen 518055, PR China

3. Department of Engineering, University of Cambridge, Trumpington Street, Cambridge CB2 1PZ, United Kingdom

Corresponding author.

***. E-mail: baorui@kmust.edu.cn (Rui Bao); **.liangliu336@163.com (Liang Liu)**

ABSTRACT

In order to uniformly disperse the ceramic reinforcements synthesized *in situ* in the copper matrix composites, this study used Carbon Polymer Dot (CPD) as the carbon source and Cu-1.0%Ti alloy powder as the matrix to supply the Ti source for manufacturing in situ synthesized TiC/Cu composites. The results showed that TiC nano-precipitate formed in the grains interior and grain boundaries, with particle sizes that were similar to the CPD size and maintained a uniform distribution state. Compared with the matrix, 0.3 wt% CPD/Cu composite displayed the best strength-plastic compatibility, the UTS had achieved to be 385 MPa accompanied with a corresponding EL of 21%. This was owing to the dislocation hindrance caused by nano-carbide and excellent interface bonding between nano TiC and the Cu matrix. The density function theory calculation had supported our experimental results, which showed a tighter and stronger interface contact. This paper presents a new approach for studying *in situ* carbide precipitates.

Keywords: copper matrix composites; in situ generation; TiC phase; Carbon Polymer

Dot (CPD); powder metallurgy

1. Introduction

Due to its excellent electrical conductivity, robust mechanical properties, and wear resistance, copper matrix composites (CMCs) have attracted increasing research interests in recent years [1-3]. CMCs are suitable for applications like electrical sliding contacts, spot welding electrodes, connectors, bearing materials and so on [4, 5]. Recent studies have demonstrated that ceramic reinforcements (such as TiC [6], TiB [7], TiB_2 [8], and Al_2O_3 [9], etc) could effectively improve the mechanical characteristics of Cu composites. TiC has been suggested as a potential reinforcement owing to its high hardness, superior thermal stability and electrical conductivity [10, 11]. Traditionally, TiC reinforcement has traditionally been mechanically mixed or blended into the matrixes [12, 13]. In fact, this *ex-situ* mixed approach is incapable of preventing agglomeration of the reinforcement (especially for the nano-scaled particles) or producing a strong enough interfacial bonding. Therefore, it is vital to introduce the reinforcements into the Cu matrix while ensuring well dispersion and strong interfacial adhesion for making high-performance TiC/Cu composites.

A novel approach of fabricating *in-situ* particulate-reinforced Cu composites utilizing pre-ceramic polymers has recently attracted a lot of interest [14, 15]. The basic principle behind this method is firstly generating carbon, boron or silicon sources by pyrolyzing polymers and then reacting them with metal matrix powders *in situ* to create reinforcements [15, 16]. The preparative technique has several attractive advantages, including improved interfacial bonding, superior dispersion and excellent chemical interface purity. For instance, incorporating silicon-based polymeric precursors into Cu matrix can fabricate the polymer-derived Cu composites [17]. Grain growth was inhibited by the *in situ* generated ceramic particles, which increased the composites hardness. Daoush et al. [18] reported that the fabrication of an Al composite reinforced with SiC and AlN could be created from SiCN powders.

Carbon polymer dots (CPDs) have a polymer/carbon hybrid structure rather than the structure of carbon main body, which contribute to the predominant properties of the CPDs [19]. CPDs have an essentially spherical shape with a size less than 10 nm.

The core is a carbon nanoparticle with sp^2 hybrid carbon atoms, and the surface has a variety of oxygen-containing functional groups, which give it exceptional water solubility and features of surface modification [20, 21]. Thus, it has better dispersibility in a copper salt solution as a colloid compared with graphene and CNTs [13, 22]. By means of the CPD as pre-ceramic polymers to fabricate *in situ* TiC particulate-reinforced Cu composites is a new strategy to improve properties. The *in situ* generated ceramic particles will inherit the incipient nano-scaled from CPD precursor (<10 nm) so the newly formed TiC nano-particles will take full advantage of the nano-size effect. In addition, due to the good dispersibility of CPD, the newly produced TiC would preserve the homogeneity with matrix. Furthermore, the *in-situ* reaction would offer strong interface bonding and chemical purity between matrix and TiC nano-particles [23, 24]. Therefore, from the perspective of dispersibility and interfacial bonding, CPD can be used as a suitable carbon precursor for *in situ* reaction of TiC nano-particles.

In this study, we constructed *in situ* TiC/Cu-Ti composites using Cu-1%wt Ti alloys matrix powders and the lab-synthesized CPD. *In situ* TiC/Cu-Ti composites were consolidated by spark plasma sintering (SPS) from hydrogen-reduced (CPD/Cu_2O)/Cu-1%wt Ti powders, in which the TiC was derived from the CPD and *in situ* reaction. The effects of reinforcement contents on microstructure and mechanical properties of composites were studied. The proposed method of using pyrolysis CPD as a precursor for *in situ* synthesized nano-scaled TiC demonstrates to be a novel way to construct high-performance Cu nanocomposites with both enhanced strength and plasticity.

2. Experiment

2.1 Synthesis of CPD

CPD was synthesized via the hydrothermal method. The citric acid (6.0 g, $C_6H_8O_7$ AR, ≥99.5%) was dissolved as a precursor in 80 ml in deionized water and then magnetically agitated for 10 minutes. After that, 1.0 ml ethylenediamine ($C_2H_8N_2$ AR, ≥98%) was injected into the solution. After full stirring in the reaction kettle, the solution, together with the kettle, was placed in a drying oven at 180℃ for 6 hours.

The resultant mixture was placed in a dialysis bag for 10 hours to purify the CPD. The purified colloidal solution was finally freeze-dried to obtain CPD powder. It should be pointed out that in our previous report, by means of the Raman spectrum and the Nuclear Magnetic Resonance Spectroscopy (^{13}C NMR), we have proved that these lab-synthetized nano sized particle was CPD [19, 21].

2.2 Preparation of the CPD/Cu-Ti composite powder

In order to reduce the size/gravity differences between CPD and Cu-1.0%wt Ti alloys powders, the molecular level mixing (MLM) method was employed by injecting CPD disperse into the copper salt solution to obtain the micro-sized CPD/Cu_2O composites powders. The CPD/Cu_2O composite powder was firstly prepared utilizing the MLM method for good CPD dispersion. Specifically, copper acetate monohydrate ($CuAc \cdot H_2O$) ($C_6H_8O_7$ AR, ≥99.5%) was dissolved in deionized water at 80 ℃. Afterwards, the well-dispersed CPD suspension was added into the salt solution to obtain a homogenous CPD/CuAc mixture. After gradually adding 9.0 g NaOH (AR, ≥99.0%) and 7.0 g glucose ($C_6H_{12}O_6$ AR, ≥99.0%) solution, the mixture was stirred until it transformed into a brick-red color. Filtering and vacuum drying were then used to make the CPD/Cu_2O composite powder.

Gas atomized pre-alloyed Cu-Ti powders with mean particles size of 13.75 μm and the purity of 99.75% (containing ~1.0 wt% solid solution Ti elements) was used as the matrix material. To improve the geometric compatibility between the cubic-shaped CPD/Cu_2O powders and Cu-1.0wt%Ti matrix powders, Cu-1.0wt%Ti powders were ball milled into flake-like powders (**Ball-milling I** in Fig. 1). Specifically, 40g Cu-1.0wt%Ti and 500 mL ethanol were sealed into a stainless jar with a 20:1 ball to powder weight ratio and ball milled at 300 rpm for 8 h under an Ar atmosphere. The lamellar Cu-1.0wt.%Ti powders were mixed with various mass fractions of the pre-prepared CPD/Cu_2O composite powder by low-energy **Ball-milling II** for 2 hours (150 r/min, 200 ml alcohol, the ball to powder ratio of 5:1). After a 6-hour hydrogen reduction at 300°C, the resultant (CPD/Cu)/Cu-Ti composite powders were obtained. Based on the thermo gravimetric analysis (TGA) [21], the final residual weight was ~27% over 600 °C

thermal degradation, which indicated the weight percentage of carbon cores in the CPD. According to the different mass fractions of the CPD in the mixed powder, the samples were designated as 0.2 CPD/Cu-Ti, 0.3 CPD/Cu-Ti, and 0.4 CPD/Cu-Ti.

2.3 Preparation of CPD/Cu-Ti bulk composite

The CPD/Cu-Ti composite powders were placed in a cylindrical graphite die for spark plasma sintering in a vacuum atmosphere (<10^{-1} Pa) at 800℃ with an axial pressure of 50 MPa. The temperature rose at a pace of 50 degrees every minute. The consolidated bulk composite was 20 mm in diameter and 5 mm in thickness. When the carbon element had completely transformed into the *in situ* synthesized TiC nano-particles, the actual TiC contents in the CPD/Cu-Ti specimens were 0.27 wt%, 0.405 wt% and 0.54 wt% for 0.2 CPD/Cu-Ti, 0.3 CPD/Cu-Ti and 0.4 CPD/Cu-Ti composites, respectively. For comparison, a Cu-Ti matrix without CPD was also manufactured under the same conditions. The preparation process of the CPD/Cu-Ti composites is depicted schematically in **Fig. 1**.

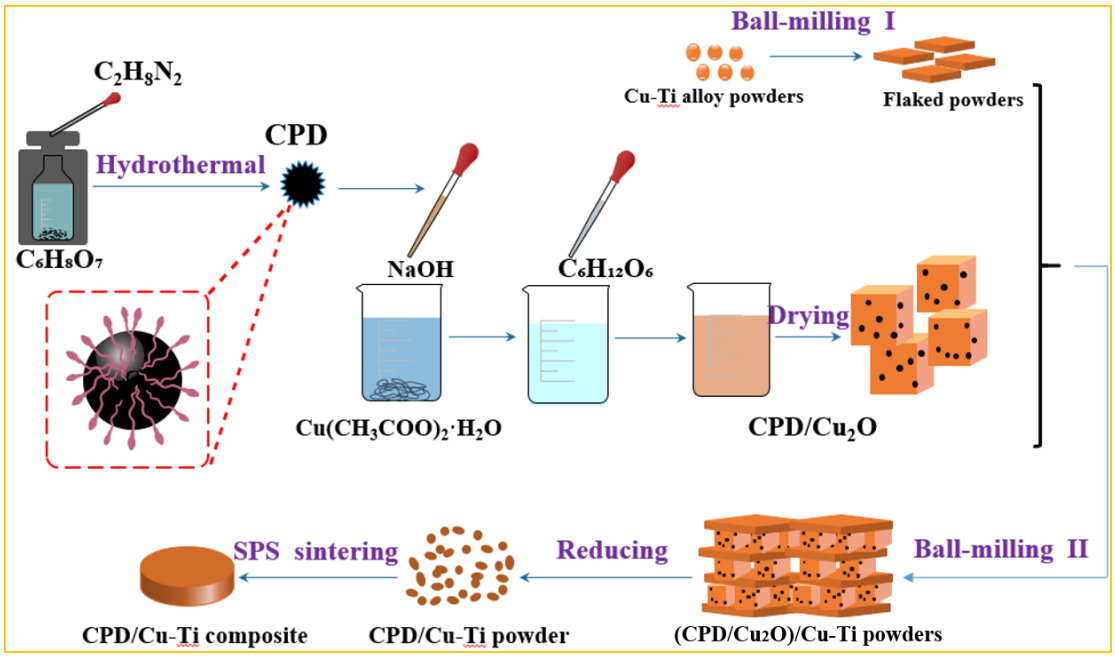

Fig. 1 Schematic diagram of the CPD/Cu-Ti composites preparation process. (SPS: spark plasma sintering; CPD: Carbon polymer dots.)

2.4 Characterization

The microstructures of the synthesized CPD and CPD/Cu_2O composites powders were fully examined using transmission electron microscopy (TEM, FEI Tecnai G2-TF30). The functional groups of the CPD were identified by Fourier transform infrared spectroscopy (FTIR, Nicolet iS 10). The carbon, oxygen and nitrogen elements of the CPD were determined by X-ray photoelectron spectroscopy (XPS, K-Alpha$^+$, Thermo Fisher Scientific). The fracture surfaces of the samples were observed by field-emission scanning electron microscopy (FE-SEM, Nova Nano450, FEI). Quasi-static tensile tests were carried out by a mechanical tester (AG-X-100 kN, SHIMADZU) at a crosshead speed of 0.2 mm/min. The bulk samples were processed into dog-bone samples with a gauge length of 10 mm and a width of 3 mm.

2.5 First principles calculations

The first-principle calculations were performed using the Vienna Ab initio Simulation Package (VASP), which was based on density functional theory (DFT) and plane-wave basis sets with periodic boundary conditions. To treat the exchange-correlation interaction of electrons, the Perdew-Burke-Ernzerhof (PBE) functional within the generalized gradient approximation (GGA) was utilized to treat the exchange-correlation energy. The electron-ion interactions were described using projector augmented wave (PAW) potentials. The irreducible wedge of the first Brillouin zone was sampled by means of the Gamma scheme using a grid of 1×1×1 for interfacial calculations. The energy cutoff for the plane-wave basis was set at 400 eV. A convergence criterion of 10^{-6} eV for the total energy and -0.02 eV/Å for the force were adopted for the self-consistent calculation and the geometry optimization, respectively.

3. Results and discussion

3.1 Microstructure of the CPD

As seen in **Fig. 2(a),** the CPDs possess spherical and ellipsoidal morphologies. Based on the particle size statistics, the average size of the CPD is ~2.39 nm, with the

smallest particle size being only 0.5 nm. The majority of the particles have a narrow range of 1.0~4.0 nm in size (see inset in **Fig. 2(a)**). In addition, both crystalline carbon and amorphous carbon can be observed in the HRTEM image (see **Fig. 2**). As shown in **Fig. 2(b$_1$)**, some of the CPD exhibit a definite crystal lattice with plane spacing of 0.207 nm, indicating a typical graphite phase of the (002) crystal plane. Meanwhile, some of them have amorphous structure characteristics (see **Fig. 2(b$_2$)**).

To learn more about the chemical composition of the CPD, a series of measurements were carried out, as illustrated in **Fig. 2(c-e)**. In the Fourier transform infrared absorption spectra, there are several noticeable absorption peaks. The stretching vibration peaks of the bending vibration of N-H are observed at ~1546 cm^{-1} and ~779 cm^{-1}. The wide absorption band at 2900~3400 cm^{-1} corresponded to the bending vibration of N-H. The characteristic peak at ~1403 cm^{-1} is the asymmetric stretching vibration of carboxylic acid anion, whereas the C=O bending vibration and N=H stretching vibration appear at ~1708 cm^{-1} and ~1652 cm^{-1}, respectively [25]. The characteristic peaks at ~2945 cm^{-1} are due to the bending vibration of -CH, and the stretching vibration peaks of hydroxyl and amine groups are observed at ~3397 cm^{-1}. A large number of surface functional groups prove that CPD has effective hydrophilicity and stability in the aqueous phase system, which is conducive to the formation of a good combination in Cu/C composite materials. The XRD spectrum of the CPD has a wide peak at approximately $2\theta=18°$, suggesting poor crystallinity of the amorphous carbon structure, as shown in **Fig. 2d**. This is consistent with the result of the HR-TEM investigation.

The full XPS spectrum clearly reveals the composition of carbon, oxygen and nitrogen elements of the CPD (see Fig. **2(e)**). High-resolution XPS of the C1 s peak (in **Fig. 2(f)**) reveals that there are not only strong C=C (sp^2) and C-C (sp^3) bonds but also C-N/C-O, C=O/C=N bonds, and O-C=O functional groups, which correspond to the C1s peaks at 283.12, 2883.96, 285.15, 286.15, and 287.61 eV, respectively. The N1s peaks in **Fig. 2g** at 398.2, 398.8, 399.4, and 400.4 eV indicate that nitrogen mainly exists in the form of C=N-O, C-N-C, C-NH_x, and N=C_3 [26, 27], respectively. The O1s

peaks at 530.2, 531.1, and 532.2 eV in **Fig. 2h** are related to O-C=O, C-O, and C=O, respectively. These findings indicate that the surface of the synthesized CPD is functionalized with multiple oxygen and nitrogen functional groups.

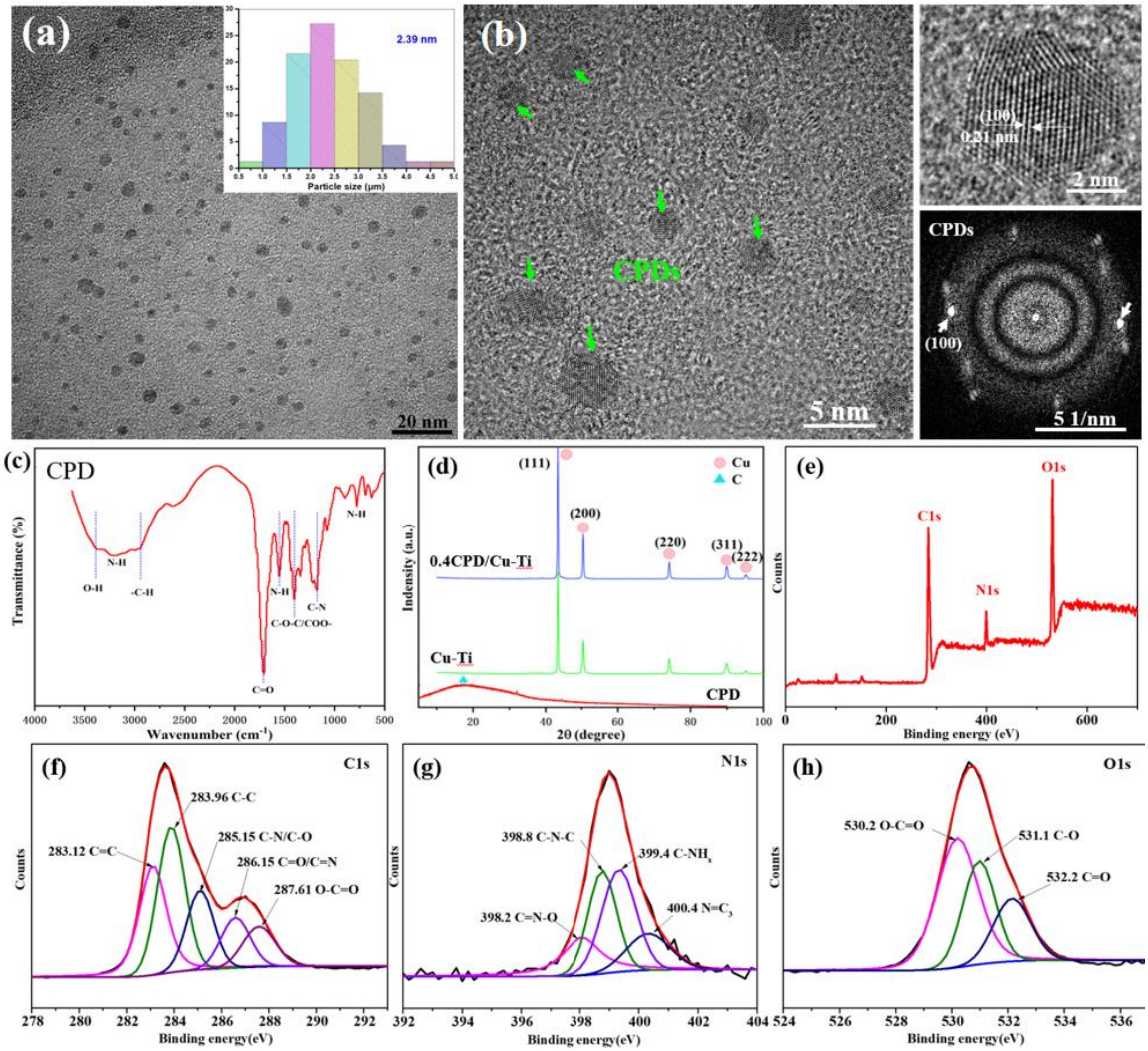

Fig. 2 (a) TEM image and histogram of the particle size distribution of the CPD, (b) HR-TEM image and corresponding Fourier diffraction spots of CPD; (c) FT-IR spectrum, (d) XRD spectra, (e) full XPS spectrum and high-resolution XPS of (f) C 1s, (g) N 1s and (h) O 1s.

3.2 Microstructure of the composite powder

Although CPD disperses well in water or other non-polar solvents, it is still challenging to be well-proportioned within the alloy matrix due to the huge density and dimensions differences with Cu-1.0wt%Ti powders. Hence, the molecular level mixing

(MLM) method was employed by adding CPD into the copper salt solution to obtain the micro-sized CPD/Cu_2O composites powders. As illustrated in **Fig. 3a**, the synthetic CPD/Cu_2O particles exhibit regular cube-like shapes, and homogenous size distribution (mean particle size ~3.35 μm). At higher magnification, it is worth noting that the edges and surface of the Cu_2O cube particles are noticeable rough, and a mass of nano-sized acicular granule attaches to it (**Fig. 3b**). However, the smooth surface of the synthesized Cu_2O particles without adding CPD, on the other hand, is shown in **Fig. 3c**. Therefore, these acicular granules are thought to be newly formed Cu_2O crystals. CPDs provide plenty of heterogeneous nucleation sites for the Cu_2O formation. These nano-sized granules represent the initial growth stage of the CPD/Cu_2O particles. After the ball milling (**I)** process, the raw spherical Cu-1.0wt%Ti powders had been transformed into flake-shaped powders with increased plane plan view size (**Fig. 3e**). Theoretically, flaked powders exhibits higher apparent volume than spherical powders of the same mass, allowing for improved surface and geometrical compatibility between cubic CPD/Cu2O and lamellar matrix powders. [28].

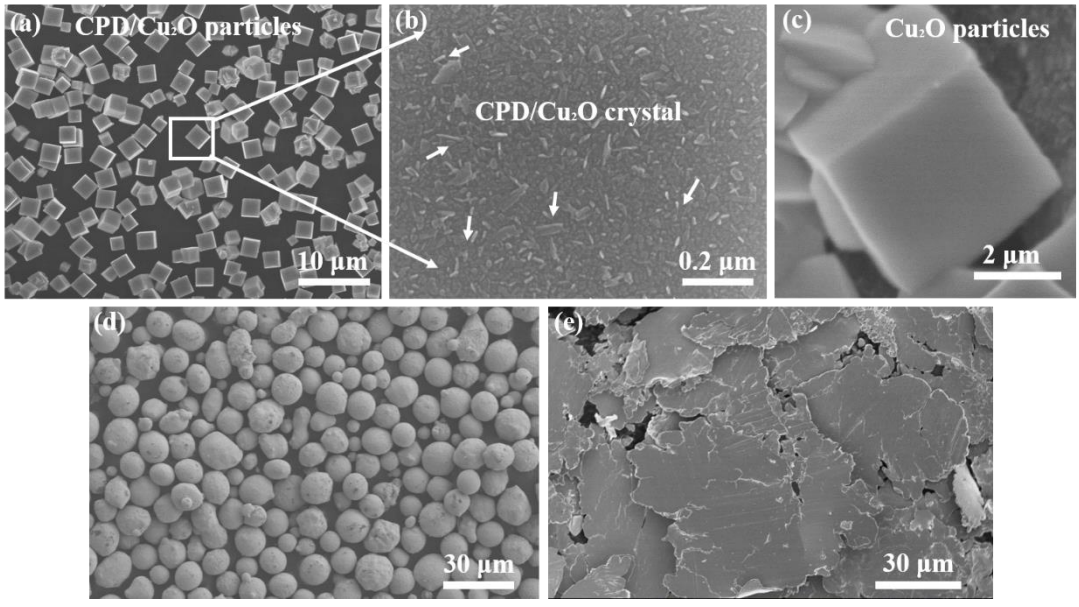

Fig. 3 (a-b) SEM images of the synthetic CPD/Cu_2O particles in different magnification, (c) Cu_2O particles without CPD additive, (d-e) morphologies of Cu-1.0wt%Ti powders before and after ball milling (**I).**

Micro-sized CPD/Cu_2O composite powders were initially created as an

intermediate product before CPD was directly added to the matrix powders during the MLM process. On the one hand, it is relatively simple to achieve the dispersion of CPD/Cu_2O in a lamellar matrix when compared to independent CPD, due to the reduced density disparity and dimensional differences with Cu-Ti powders. On the other hand, the uniformly distributed micron-sized particles can ensure the dispersion properties of CPD and suppress the possible secondary agglomeration of the CPD. In brief, such an intermediate product plays an important role for the homogeneous dispersion of CPD. **Figs. 4(a-b)** show the morphologies of (CPD/Cu_2O)/Cu-Ti mixed powders after mixing by low-energy ball milling **(II)**. CPD/Cu_2O particles are uniformly distributed on the lamellar powder surface in the magnified image. The relatively "hard" and tiny oxide particles (CPD/Cu_2O) are inclined to stick to the "soft" matrix powders, similar to how sesame seeds attach to biscuits.

Figs. 4(c-e) show the morphologies of resultant (CPD/Cu)/Cu-Ti composite powder after 6 hours hydrogen reduction in flowing H_2-N_2. In contrast to their original cubic morphology, the bulk of CPD/Cu particles take on an irregular shape. The newly reduced CPD/Cu particles display more compact adhesion with the underneath lamellar matrix powders, and a fraction of these particles looks like fuse together with the lamellar Cu-Ti powder via the thermal diffusion (see **Fig. 4c**). The deep void in CPD/Cu particles is the escape channel of oxygen element (see **Fig. 4d**). Of particular note is CPD maintained an even distribution on the surface and embed inside of the Cu particles, creating an ideal interface adhesion state (see **Fig. 4e)**. Overall, the above-mentioned analysis indicates that the CPD/Cu_2O composite powders prepared by MLM most likely disperse CPD within flaked Cu-Ti matrix powders in an effective way, resulting in enhanced interface bonding with the reduced Cu particles.

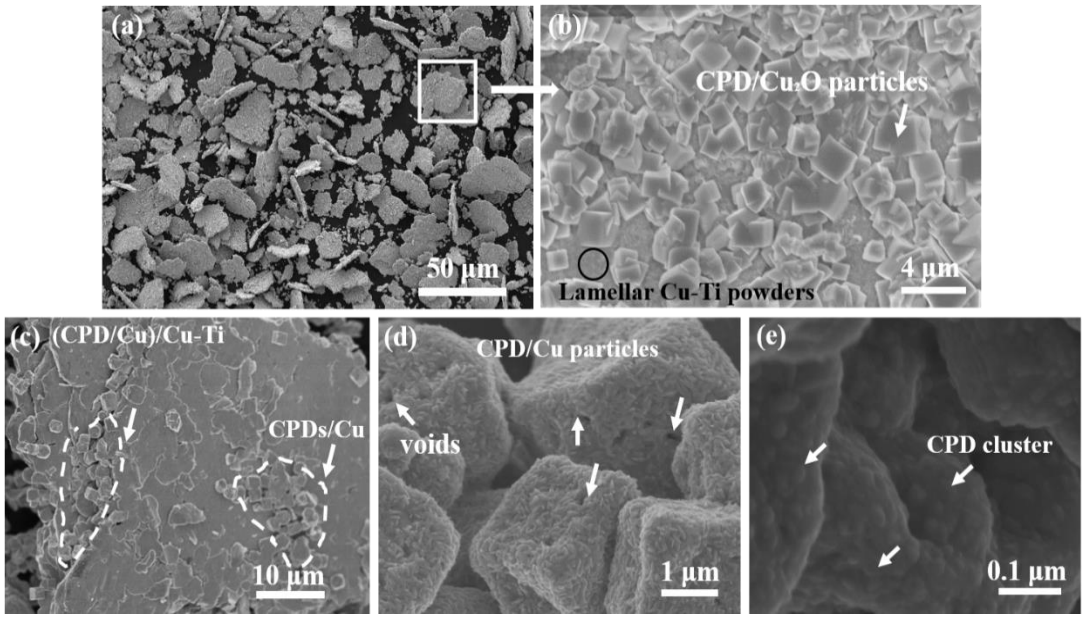

Fig. 4 SEM images of (a-b) the (CPD/Cu_2O)/Cu-Ti powder after ball milling (**II**), (c-e) the morphologies of (CPD/Cu)/Cu-Ti powder after hydrogen reduction

3.3 Interface structure of bulk composite

The interface structure of the 0.2 CPD/Cu-Ti composite was further investigated using TEM, as shown in **Fig. 5**. The uniform dispersion of nano-particles (indicated by the arrows) distributed in the Cu-Ti matrix has proved that no agglomeration of CPD precursor was achieved. An enlarged view of the selected blank is shown in **Fig. 5(b),** these nano-particles have a high degree of crystallinity in contrast to the initial CPD (with the amorphous structure characteristics). The HRTEM image in **Fig. 5(c)** depicts that the interface state between the matrix and nano-particles is close-knit without any voids, indicating that the interface adhesion is sufficiently robust. The gray contrast of nano-particles has a significant difference with the adjacent matrix; therefore, the atom-scaled HRTEM image is obtained through carefully adjusting the incident zone axis of [110] for FCC crystal structure. The typical lattice fringes of titanium carbide (111) and (200) planes with inter-planar crystal spacing of 0.249 nm and 0.216 nm are marked in the HRTEM image, as shown in **Fig. 5(d)**. The calibration of the diffraction spots shows the presence of TiC, which has a cubic structure of space group Fm-3m corresponding to a unit cell parameter of a=0.432 nm [29, 30]. Both the lattice fringes and FFT calibration analysis have verified that these nano-particles are *in-situ* produced TiC phase, which

occurred via the C-Ti reaction diffusion mechanism. The selected area electron diffraction (SAED) pattern in the nanobeam diffraction (NBD) mode of TEM was used to analyze the TiC-Cu interface structure (the NBD pattern is shown in **Fig. 5(e))**. The orientations relationship of Cu-TiC interface: Cu(022)//TiC (111) & Cu(2-20)//TiC(002) demonstrates a strong interface bonding between matrix and TiC nano-particles.

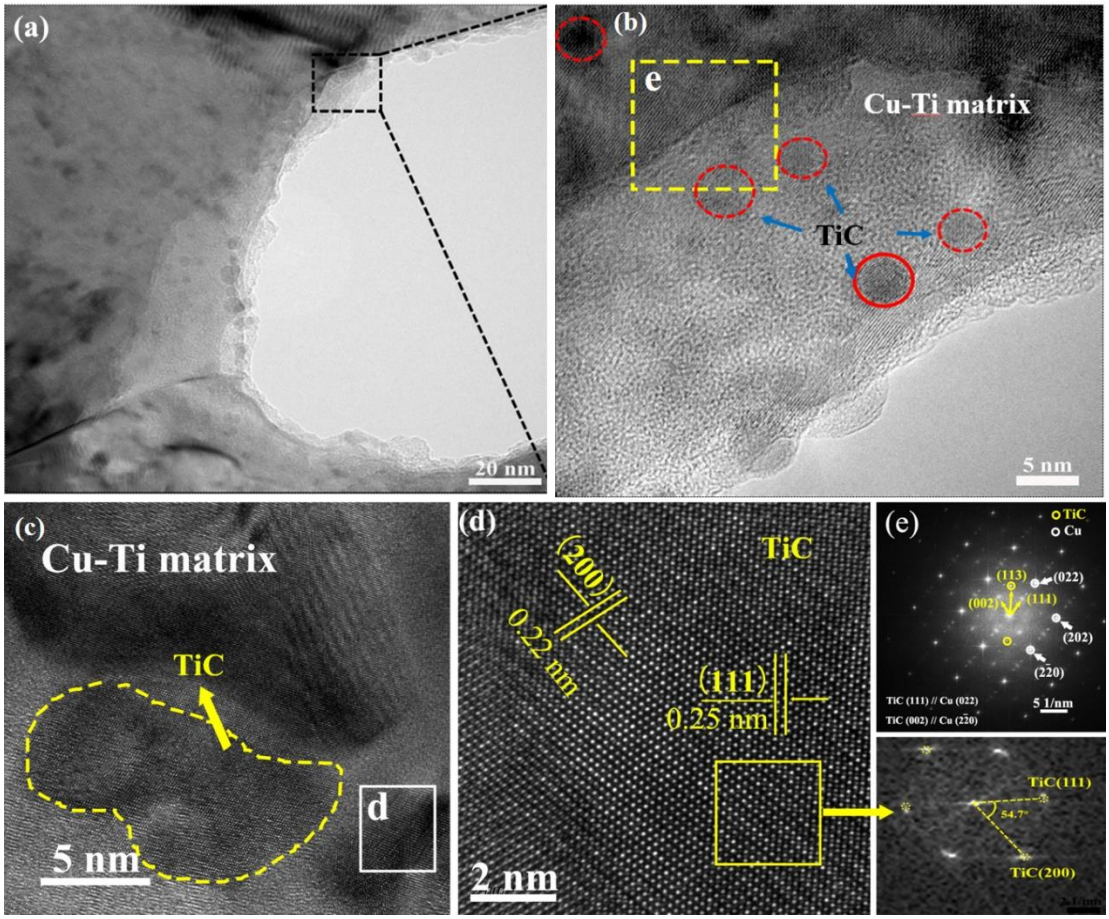

Fig. 5 TEM images of the 0.2 CPD/Cu-Ti composite: (a) the overall morphology, (b-c) HRTEM images shows the interface structure between TiC nano-particles and matrix, (d) atom-scaled HRTEM image of TiC and the relevant FFT image, (e) SAED pattern in the nanobeam diffraction (NBD) mode.

Based on the microstructural studies, the possible formation and evolution process of the in-situ formed TiC nano-particles is proposed. During the sintering process, CPD decompose into carbon cores and uniformly distributed in the Cu grain boundaries. The carbon-enriched areas (concentrated at the grain boundaries) would alter the chemical potential gradients for titanium atoms diffusion. Thus, due to the strong electrophilic of

Ti and C elements, Ti atoms would diffuse toward to the carbon-enriched areas and then react with thermally activated carbon atoms, it is strongly electrophilic and reactive to form Ti-C ionic bonds. On the other hand, there are sufficient sp^3 C-C dangling bond on the CPD surface, the activated carbon atoms are easier to diffuse into Cu-Ti matrix as an interstitial atom, triggering the solid-state process and creating the TiC nucleus. Due to the low solid solubility of carbon atoms within Cu matrix, the TiC nucleus would precipitate out of the matrix and gradually form TiC nano-particles. Thus, in-situ TiC formation is a thermally induced and diffusion-controlled process in the solid state. As time increases, the diffusion of carbon and titanium atoms eventually reach equilibrium, and all the CPD are transformed to TiC phases.

3.4 Mechanical properties and fractured morphologies

The engineering stress-strain tensile curves of CPD/Cu-Ti composites and Cu-Ti matrix are presented in **Fig. 6(a)**, which reveal a mass fraction-typed dependence on mechanical properties. The contents of the TiC nano-particles increase with the CPD content. The measured yield strength (YS), ultimate tensile strength (UTS) and elongation (EL) of the Cu-Ti matrix are 242 MPa, 274 MPa, and 26.5%, respectively. In comparison to matrix counterparts, CPD/Cu-Ti composites have better mechanical properties (YS & UTS). For the 0.2 CPD/Cu-Ti composite, the plasticity has reduced somewhat but the UTS has increased by 31 MPa as compared to the Cu-Ti matrix. 0.3 CPD/Cu-Ti composite displays the best strength-plastic compatibility, the UTS has achieved to be 385 MPa with a corresponding EL of 21%. With the further increase of CPD content, both the UTS and EL have decreased dramatically. It shows that the mechanical properties of CPD/Cu-Ti composites are largely sensitive to the quantity of CPD addition. The main reasons for the decline of the enhancement effect with high content of CPD introduction are due to the formation of excess unreacted CPD and agglomerated TiC. Therefore, a reasonable addition should be maintained at 0.3wt.% in this study.

Furthermore, the fractured morphologies of 0.3 CPD/Cu-Ti and 0.4 CPD/Cu-Ti composites are shown in **Figs. 6(b-c)**, respectively. In low magnification images of the

two composites, the representative ductile fracture with innumerable dimples over the entire fractured surface can be observed. However, local areas marked by the boxes in **Fig. 6(c)** demonstrate where heavily agglomerated TiC particles are separated from the matrix. This is because effectively scattering CPD precursors within the metal matrix gets more challenging as the weight percentages of CPD precursors in the composite matrix increase. The found weak interfacial bonding between the matrix and the reinforcement affected the overall mechanical properties of the 0.4 CPD/Cu-Ti composite.

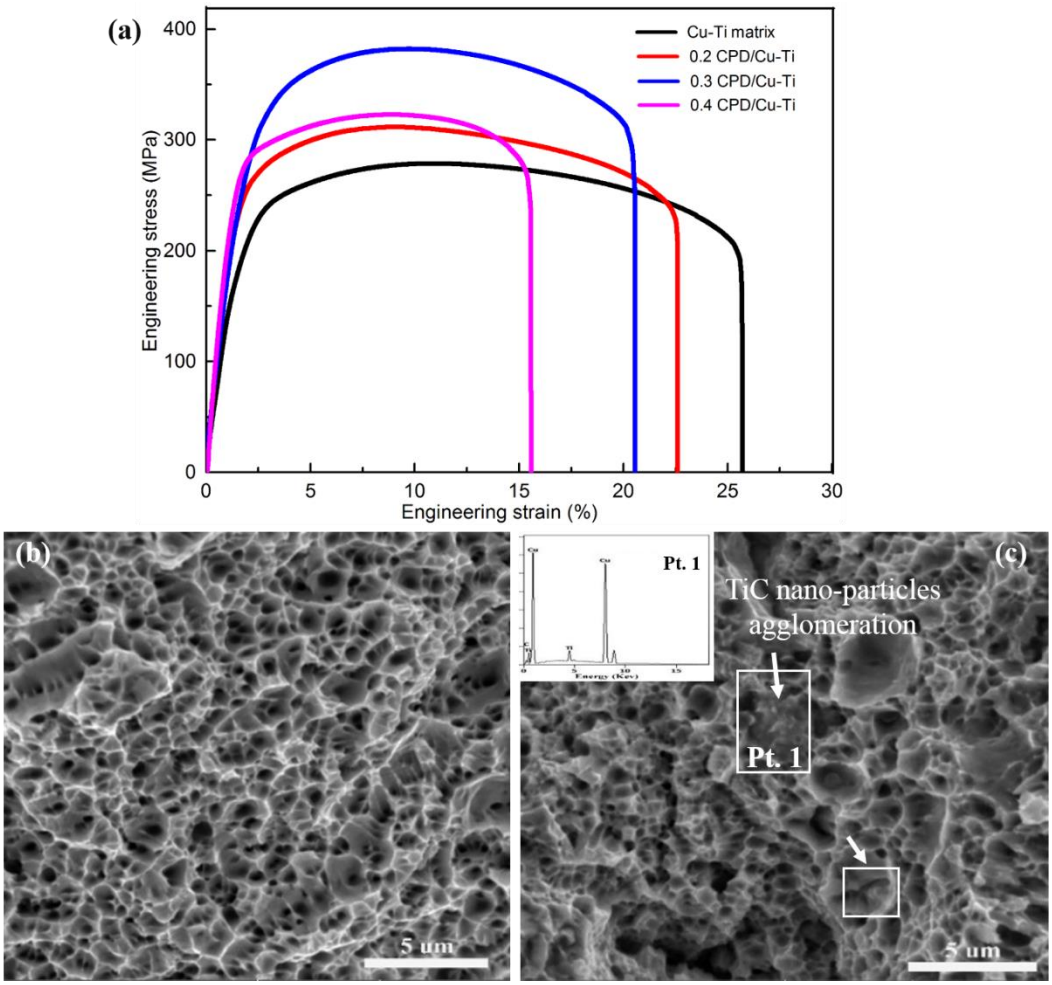

Fig. 6 (a) Engineering stress–strain tensile curves of CPD/Cu-Ti composites and Cu-Ti matrix; the fractured morphologies of (b) 0.3 CPD/Cu-Ti and (c) 0.4 CPD/Cu-Ti composite.

The significant strength improvement of CPD/Cu-Ti composites is mainly ascribed to the homogenous distribution of *in-situ* generated TiC nano-particles. To

begin with, TiC particles formed *in situ* at grain borders may obstruct grain growth, resulting in a significant decrease in grain size. Statistical results show that the average grain size of 0.3 CPD/Cu-Ti composite is 1.14 μm, while it is 1.80 μm for the unreinforced Cu-Ti matrix, more detailed information is provided in the Supplementary Material. Thus, the contribution arising from grain refinement to the Cu-Ti matrix cannot be neglected. Second, TiC nano-particles increases the strength mainly via the Orowan looping mechanism. The Orowan looping system is related to dislocation movement and occurs during plastic deformation, leading to a visible contribution to dislocation strengthening. Finally, the thermal expansion mismatch between in situ generated TiC particles and Cu-Ti matrix could produce extra dislocations in the robust interface region. The increasing dislocation density within the matrix strengthens the composite. Therefore, the overall strengthening effects of the composites are closely related with the strong interfacial bonding stemming from the *in-situ* synthesized TiC nano-particles [31]. Although the EL of CPD/Cu-Ti composites declined somewhat as CPD content increased, they still maintained a good strength-ductility ratio. It is assumed that the *in-situ* synthesized TiC nano-particles has replaced the uniformly dispersed CPD, which can effectively improve the load transfer ability loaded on the composite. In addition, TiC nano-particles can impede or delay the crack propagation through the bridging effect. In addition to the mechanical properties improvement, the thermal conductivity of CPD/Cu-Ti composites is also an important focus in our study. But further studies are required to elucidate the interfacial bonding on the effect of CPD/Cu-Ti composites' thermal conductivity in our later work.

3.5 Simulation verification

We properly conclude that Ti has entirely precipitated from the Cu-Ti matrix after sintering, leaving only copper in the matrix based on the TEM observation result. Additionally, when creating a periodic crystal structure using the first principle, copper structure is better in line with experimental findings and the creation of a theoretical interface than Cu-Ti alloy structure. We calculated the separation distance (d_0) between Cu(110) and TiC(110) slabs in the initial condition of the interface by estimating the

binding strength of the interface at various interfacial distances and fitting it with the universal binding relation (UBR). The amount of energy needed per unit area to reversibly separate an interface into two free surfaces is defined as work of adhesion, also known as interfacial binding energy. In this study, the work of adhesion is calculated for unrelaxed interfacial structures using Eq. (1)[32]:

$$W_{bind} = (E_{cu\_slab} + E_{TiC\_slab} - E_{cu/TiC})/2A \quad (1)$$

where E_{Cu_slab}, E_{TiC_slab} are the total energies of a seven-layer Cu(110) and seven-layer TiC(110) free surfaces with the same lateral lattice parameters as the Cu/TiC interface; $E_{Cu/TiC}$ is the total energy of interface; A refers to the interfacial area, and the factor of two in the denominator accounts for the two identical interfaces in the supercell. For the relevant energies in Eq. (1), all first principles calculations were non-spin polarize. This procedure offers a reliable estimate of the initial d_0 value between Cu and TiC slabs in the supercell models for all interfaces. We were able to determine the binding energies by increasing the separation distance d between two rigid free surfaces from 1.4 to 3.4 Å. The obtained W_{bind} versus d is shown in **Fig. 7**. Here, the optimal d_0 is calculated using the lowest value in each W_{bind} versus d profile. Since all obtained profiles of work of adhesion exhibit a single minimum as a function of separation distance d, the UBR can be used to fit the data. The universal binding relation used in this research is given by Eq. (2)[33].

$$W_{bind}(\chi) = Wc[1 + \frac{x-d_0}{l}]exp\ (-\frac{x-d_0}{l}) \quad (2)$$

Here, the fitting parameters Wc and d_0 define the maximum in the work of adhesion profile with the rigid slab approximation; l is mainly served as a fitting constant with the same dimensionality to the separation distance d.

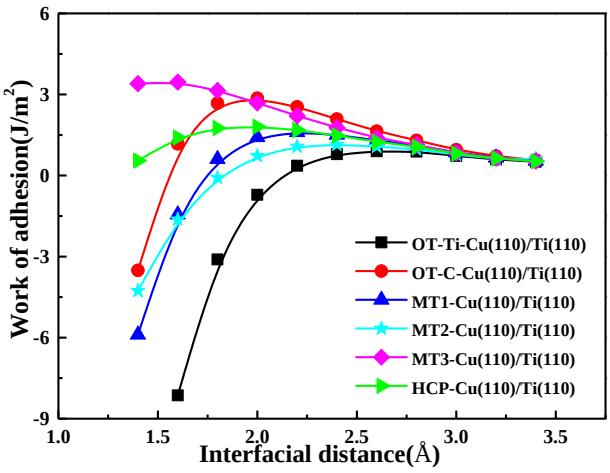

Fig. 7 Interfacial binding as a function of separation distance between TiC and Cu slabs for different interfacial configurations of interfaces.

As shown in **Fig. 8**, six possible atomic stacking sequences for TiC(110)/Cu(110) interface (OT-Ti, OT-C, MT1, MT2, MT3 and HCP) are illustrated. OT-Ti is the Cu atom at the top position of the Ti atom on the TiC side; OT-C is the Cu atom at the top position of the C atom on the TiC side; MT1 is the Cu atom at the bridge position of Ti and C atoms on the TiC side; MT2 is the Cu atom at the bridge site of Ti atom on TiC side; MT3 is the bridge site where Cu atom is on carbon atom, HCP site is where Cu atom is in vacancy.

All relaxed interface configuration (OT, MT and HCP) of TiC(100)/Cu(110) are shown in **Fig. 8**. For the OT-Ti, OT-C, MT2 and HCP configurations, structural relaxation has no effect on interface atomic structure, indicating that the above configuration is structurally stable. **Fig. 8(c)** show that structural relaxation has a significant effect on MT1 configuration, the Cu atom occupying the bridge between Ti and C move to on the top of outmost C atoms, leading to the Cu-C bonding is formed at the interface. Furthermore, the **Fig. 8(f)** reveal that the Cu of hollow site convert into the bridge between C and C atomic, implying that the HCP configuration is unstable compared with the MT3 configuration. After structural optimization, structural reconstructions at interface for the MT1 and HCP are clearly shown in **Fig. 8**. The change of the MT1 structure into the OT-C structure and the HCP structure into the MT3 structure demonstrates the instability of these two configurations. According to

the d_0 and W_{ad} value before and after relaxation in **Tab.1**, we choose the MT2 which has the maximum W_{ad} value as the most stable structure for calculating mechanical properties.

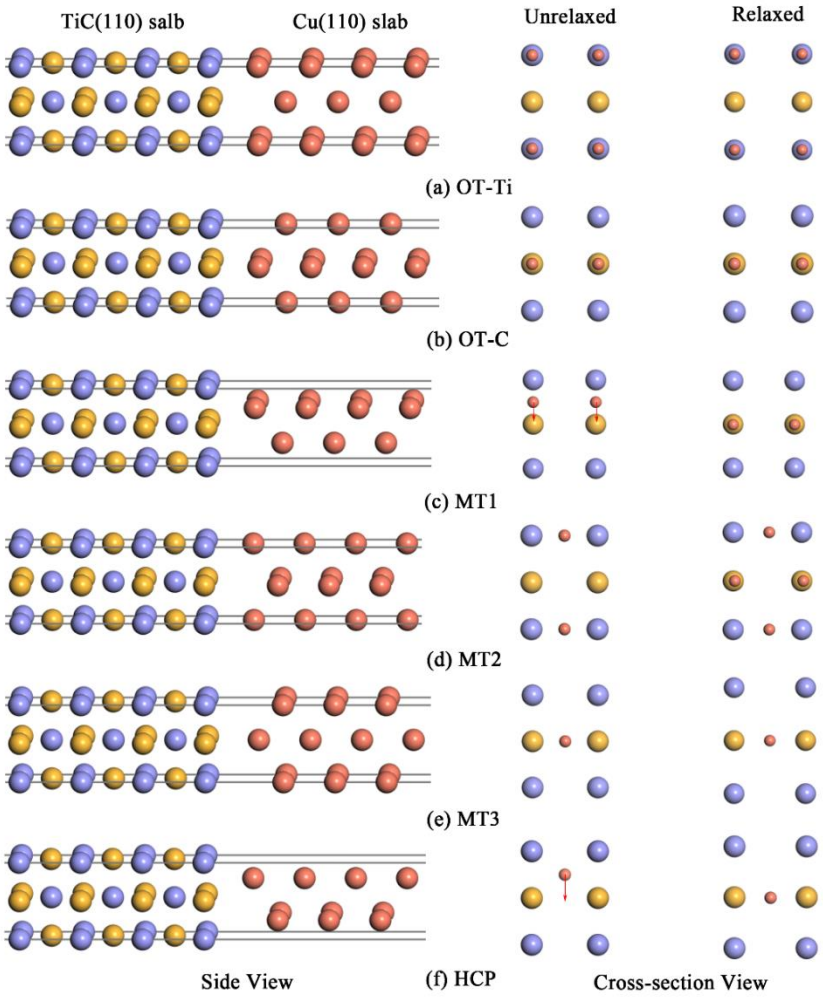

Fig. 8 Interfacial atomic structure of the Cu(110)/TiC(110) interface. (a) OT-Ti (b) OT-C (c) MT1 (d) MT2 (e) MT3 and (f) HCP. The left figure is the side view of interface stacking sequences; atoms in the green contributes to the main interfacial reconstruction. The center and right figures refer to top view of interfacial structures before and after optimization, respectively. The Ti, C, and Cu atoms are shown as purple, yellow and orange balls, respectively.

Table 1 Calculation interfacial parameters of the models: interface spacing and the work of adhesion.

Termination	Stacking	Unrelaxed		Relaxed	
		d_0 (Å)	W_{ad}(J/m^2)	d_0 (Å)	W_{ad}(J/m^2)
Cu(111)/Gr(001)	TOP	3.1	0.285	3.077	0.290
Cu(110)/TiC(110)	OT-Ti	2.6	0.897	2.556	7.665
	OT-C/MT1	2.0	2.864	1.927	4.571
	MT2	**2.4**	**1.148**	**2.281**	**8.868**
	MT3/HCP	1.6	3.457	1.244	6.833

In the first principle tensile experiment, the normal strain is applied directly to the fully relaxed interfacial supercell model in the z-direction. In this way, the ideal tensile strength of the interface might be achieved. The relationship between tensile stress and strain on the z-axis demonstrates one possible way to depict the strength of interface bonding. Interface bonding holds the key to enhancing the properties of graphene-copper or carbon nanotube-copper composites. The normal strain is given by **Eq. (3)** in terms of engineering strain [34].

$$\varepsilon_{tensile} = (l - l_0)/l_0 \tag{3}$$

Where l_0 and l denote the original and the deformed cell lengths, respectively. The engineering strain is created and applied to the interfacial supercell model in a quasi-static way. In this procedure, the strain is gradually raised by 0.1%. At each stage, the supercell model is only allowed to relax the atomic position in the structure. Meanwhile, the lateral lattice parameters of the supercell are all fixed. As a result, in all our calculations, we ignore Poission contractions in the directions parallel to the interface. More importantly, the supercell of preceding stage is employed in each subsequent step until the tensile experiment approaches mechanical failure.

For comparison, we calculated the stress-strain relationship of pure copper in

different tensile directions. The ideal stress-strain is produced by the perfect crystal structure created in line with the first principle. The stress-strain differs from the real stress-strain because the effects of dislocation slip, impurities, vacancies, and other flaws are not taken into consideration. Stretching pure copper samples in various directions yields the highest ideal tensile strength and elongation of 25.9 GPa and 26.9%, respectively, whereas the composite interface's tensile strength and elongation may reach 38.1 GPa and 29.4%, respectively. Even if the real tensile strength is linked to the defect form and existing state in the material, the ideal tensile curve may qualitatively describe the impact of interfacial bonding in the crystal on the tensile strength. As illustrated in **Fig. 9a**, the heterogeneous interface between TiC and copper is conducive to improving the matrix's mechanical properties.

To further verify the interface bonding, the charge density difference of the interface region, which can effectively reveal the electron transfer created by the formation of interface, are calculated. The in situ formed TiC is smaller and more dispersible because of the high activity, tiny size, and improved dispersibility of the CPD. If the graphene is not entirely reacted, however, there is still a contact between the copper and graphene in the composite. Hence, for comparison, both the Cu/graphene and Cu/TiC interfaces are calculated and shown in **Fig. 9(b-c)**. The expression can be indicated as $\Delta\rho_1 = \rho_{interface} - (\rho_{Cu\_slab} + \rho_{graphene\_slab})$, $\Delta\rho_2 = \rho_{interface} - (\rho_{Cu\_slab} + \rho_{TiC\_slab})$, where $\rho_{interface}$ is the electron density of the interface structure, ρ_{Cu_slab}, $\rho_{graphene\_slab}$ and ρ_{TiC_slab} are the unperturbed electron densities of the Cu, graphene and TiC slabs, respectively.

According to our observations, electron transfer at Cu/TiC interface is significantly higher than that at the Cu/graphene interface. The electrons accumulation at the Cu/TiC interface is one-order-of-magnitude higher than that of Cu/graphene, indicating that the Cu/TiC interface has stronger electron interaction than Cu/graphene. Due to the interface interaction, the first layer of carbon atoms in TiC slab also has obvious charge transfer. This electron correlation effect, on the other hand, has a wider range and can be extended to the second even third layer of the copper atoms. Under

different strain states, the Cu/TiC interface fracture surface occurs preferentially between the Cu crystal planes rather than between the Cu/TiC interface, suggesting that the interface bonding between the two slabs is stronger.

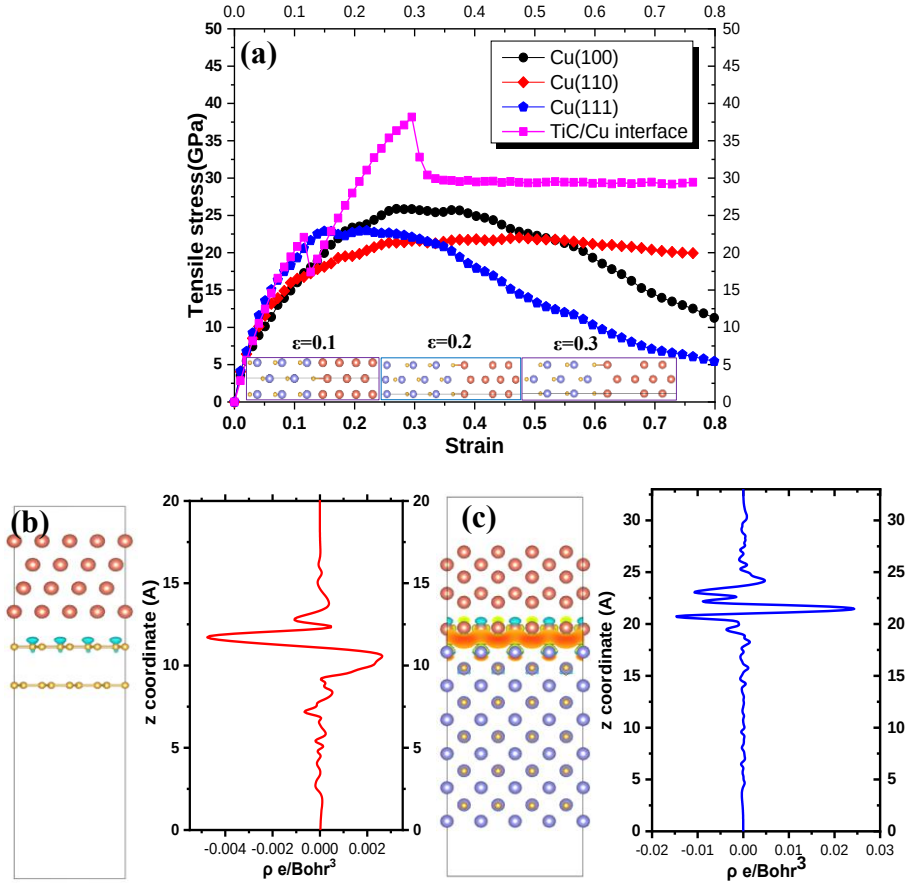

Fig. 9 (a) Profiles of tensile stress versus engineering strain of pure Cu and TiC(110)/Cu(110) interface. Charge Density Difference (e/Bohr^3) of models (b) Cu/pristine graphene, (c) Cu/TiC. Isosurface value of the structures is 0.001 e/Å^3, where the accumulation and depletion of electrons are indicated in yellow and green, respectively. The Ti, C, and Cu atoms are shown as purple, yellow and orange balls, respectively.

4. Conclusion

This work prepared copper matrix composites by *in situ* generation of the nano TiC phase using CPD as the carbon source. The compatibility of strength and plasticity of the composites were enhanced obviously, which can be ascribed to the strong interfacial bonding created by the *in-situ* synthesized TiC nano-particles. Theoretical

calculations also revealed that the Cu/TiC interface had a higher ideal tensile strength than that of a copper matrix. Our findings proved that it was feasible to employ CPD as a carbon source to reinforce the Cu-Ti matrix by the *in-situ* generation of TiC nanoparticles and implied how to improve the strength and plasticity of copper-based materials simultaneously.

Acknowledgment

This work is supported by the Chinese National Science Foundation (Grant No. 52174345, 52064032) and the Yunnan Science and Technology Projects (Grant No. 202002AB080001). Science and Technology Major Project of Yunnan Province (Grant No. 202202AG050004).

References

[1] L. Liu, R. Bao, J.H. Yi, C.J. Li, J.M. Tao, Well-dispersion of CNTs and enhanced mechanical properties in CNTs/Cu-Ti composites fabricated by molecular level mixing, J. Alloy. Compd. 726(2017) 81-87.

[2] X. Zhang, C.S. Shi, E.Z. Liu, F. He, L.Y. Ma, Achieving high strength and high ductility in metal matrix composites reinforced with a discontinuous three-dimensional graphene-like network, Nanoscale. 9(2017) 11929-11938.

[3] X. Zhang, C.S. Shi, E.Z. Liu, F. He, L.Y. Ma, Q.Y. Li, In-situ space-confined synthesis of well-dispersed three-dimensional graphene/carbon nanotube hybrid reinforced copper nanocomposites with balanced strength and ductility, Compos. Part A-Appl. S. 103(2017) 178-187.

[4] M. Cao, D.B. Xiong, Z.Q. Tan, G.L. Guo, Z.Q. Li, D. Zhang, Aligning graphene in bulk copper: Nacre-inspired nanolaminated architecture coupled with in-situ processing for enhanced mechanical properties and high electrical conductivity, Carbon. 117(2017) 65-74.

[5] M. Yang, Y. Liu, T.X. Fan, D. Zhang, Metal-graphene interfaces in epitaxial and bulk systems: A review, Prog. Mater. Sci. 110(2020) 100652.

[6] K. Rajkumar, S. Aravindan, Tribological performance of microwave sintered copper–TiC–

graphite hybrid composites, Tribol. Int. 44(2011) 347-358.

[7] Y.H. Jiang, D. Li, S.H. Liang, Phase selection of titanium boride in copper matrix composites during solidification, J. Mater. Sci. 16(2017) 2957-2963.

[8] Y. Shu, Y.N. Xiong, X. Luo, Z.B. Zhang, Adhesion strength, stability and electronic properties of TiB_2 reinforced copper matrix composites: A first principles study, Physica B. 625(2021) 413457.

[9] M.K. Singh, R.K. Gautam, Synthesis of Copper Metal Matrix Hybrid Composites Using Stir Casting Technique and Its Mechanical, Optical and Electrical Behaviours, Transactions of the Indian Institute of Metals. 70(2017) 2415-2428.

[10] L. Liu, Y.K. Li, H.M. Zhang, Enhanced strain-hardening capability in graphene nanoplatelets reinforced Ti composites through tailoring a novel three-dimensional interface structure, Compos. Part A-Appl. S. 156(2022) 106892.

[11] L. Liu, Y.K. Li, H.M. Zhang, X.W. Cheng, Good strength-plasticity compatibility in graphene nanoplatelets/Ti composites by strengthening the interface bonding via in-situ formed TiB whisker, Ceram. Int. 47(2021) 4338-4343.

[12] GH.A. Bagheri, The effect of reinforcement percentages on properties of copper matrix composites reinforced with TiC particles, J. Alloy. Compd. 676(2016) 120-126.

[13] L. Liu, R. Bao, J.H. Yi, Mono-dispersed and homogeneous CNT/Cu composite powder preparation through forming Cu_2O intermediates, Powder Technol. 328(2018) 430-435.

[14] G. Zhang, J.D. Guo, H. Chen, Y. Cao, Organic mesh template-based laminated object manufacturing to fabricate ceramics with regular micron scaled pore structures, J. Eur. Ceram. Soc. 41(2020) 2790-2795.

[15] E. Molero, B. Ferrari, A.J. Herencia, E. Gordo, Ti/Ti_3SiC_2(/TiC) Bulk and Foam Composites by Pyrolysis of Polycarbosilane and TiH_2 Mixtures, Adv. Eng. Mater. 19(2017) 1600700.

[16] X. Lu, Y. Pan, W.B. Li, M.D. Hayat, F. Yang, High-performance Ti composites reinforced with in-situ TiC derived from pyrolysis of polycarbosilane, Mat. Sci. Eng. A. 795(2020) 139924.

[17] E. Castellan, A. Molinari, A Novel In Situ Method for Producing a Dispersion of a Ceramic Phase into Copper That Remains Stable at $0.9T_M$, Metall. Mater. Trans. A. 27(2013) 4734-4742.

[18] W. Daoush, A Francis, Y. Lin, R. German, An exploratory investigation on the in-situ synthesis of SiC/AlN/Al composites by spark plasma sintering, J. Alloy. Compd. 622(2015) 458-462.

[19] W.M. Zhao, R. Bao, J.H. Yi, Influence of carbonized polymer dot (CPD) structure on

mechanical and electrical properties of copper composite, Mater. Charact. 181(2021) 111463.

[20] W. Zhao, R. Bao, J.H. Yi, Y. Zhang, Achieving a better mechanical enhancing effect of carbonized polymer dots than carbon nanotubes and graphene in copper matrix, Compos. Commun. 28(2021) 100906.

[21] W.M. Zhao, R. Bao, J.H. Yi, D. Fang, C.J. Li, J.M. Tao, Improving mechanical and thermal property of pure copper matrix simultaneously by carbonized polymer dots (CPD) cluster reinforcement, Mat. Sci. Eng. A. 805(2021) 140573.

[22] L. Liu, R. Bao, J.H. Yi, D. Fang, Fabrication of CNT/Cu composites with enhanced strength and ductility by SP combined with optimized SPS method, J. Alloy. Compd. 747(2018) 91-99.

[23] L.J. Huang, Q. An, L. Geng, S. Wang, S. Jiang, X.P. Cui, Multiscale Architecture and Superior High-Temperature Performance of Discontinuously Reinforced Titanium Matrix Composites, Adv. Mater. 33(2021) 2000688.

[24] Q. An, L.J. Huang, B. Zhong, L. Geng, Intergrowth microstructure and superior wear resistance of (TiB + TiC)/Ti_{64} hybrid coatings by gas tungsten arc cladding, Mater. Design. 162(2019) 34-44.

[25] T. Ghodselahi, M.A. Vesaghi, A. Shafiekhani, XPS study of the Cu@Cu_2O core-shell nanops, Appl. Surf. Sci. 255(2008) 2730-2734.

[26] S.Y. Tao, Y.B. Song, S.J. Zhu, A new type of polymer carbon dots with high quantum yield: From synthesis to investigation on fluorescence mechanism, Polymer. 116(2017) 472-478.

[27] Y. Yu, P.X. Tang, B. Barnych, C.Y. Zhao, Design and Synthesis of Core-Shell Carbon Polymer Dots with Highly Stable Fluorescence in Polymeric Materials, ACS Appl. Nano Mater. 10(2019) 6503-12.

[28] Y.Y. Jiang, Z.Q. Tan, R. Xu, G.L. Fan, Tailoring the structure and mechanical properties of graphene nanosheet/aluminum composites by flake powder metallurgy via shift-speed ball milling, Compos. Part. A-Appl. S. 111(2018) 73-82.

[29] L Liu, Y.K. Li, H.M. Zhang, X.W. Cheng, Breaking through the dynamic strength-ductility trade-off in TiB reinforced Ti composites by incorporation of graphene nanoplatelets, Compos. Part. B-Eng. 230(2022) 109499.

[30] L. Liu, Y.K. Li, H.M. Zhang, X.W. Cheng, Graphene nanoplatelets (GNPs)-templated synthesis of oriented TiB and the inspiration for tailoring three-dimensional (3D) interface structure in GNPs/Ti matrix composites, Mater. Charact. 181(2021) 111447.

[31] L. Liu, Y.K. Li, H.M. Zhang, X.W. Cheng, X.N. Mu, Simultaneously enhancing strength and ductility in graphene nanoplatelets reinforced titanium (GNPs/Ti) composites through a novel three-dimensional interface design, Compos. Part. B-Eng. 216(2021) 108851.

[32] Liu L, Bao R, Zhao W, Vacant defect and nitrogen doping effects on the interface of graphene/Cu composites: Computational and experimental evaluation, J. Alloy. Compd. 907(2022) 164531.

[33] Y.F. Li, B. Xiao, G.L. Wang, L. Sun, Revealing the novel fracture mechanism of the interfaces of TiB_2/Fe composite from a first principles investigation, Acta. Mater. 156 (2018) 228-244.

[34] L.L. Wu, R.F Tian, B. Wan, H.Y. Liu, N. Gong, Prediction of Stable Iron Nitrides at Ambient and High Pressures with Progressive Formation of New Polynitrogen Species, Chem. Mater. 23 (2018) 8476-8485.